International Journal of Enhanced Research in Science, Technology & Engineering
ISSN: 2319-7463, Vol. 15 Issue 5, May-2026

Comparative Analysis between Green Combustion and Microwave-Assisted Synthesis of Sm^{3+}-Activated Molybdates Nanophosphors: Structural and Luminescence Investigations

Diksha[1], Sweety Verma[2], Heena Dahiya[3]

[1,3]Department of Chemistry, Baba Mastnath University, Asthal Bohar, Rohtak, Haryana, 124021, India
[2]Chemical Process Solution Research Centre, Korea Research Institute of Chemical Technology (KRICT), Daejeon, 34114, South Korea

Corresponding author: Dr. Heena Dahiya, E-mail address: heena@bmu.ac.in

ABSTRACT

In the present work, pure and Sm^{3+}-activated Gd$_2$MoO$_6$ (0.5 mol%) nanophosphors were synthesised via an eco-friendly solution combustion route employing aloe vera extract as a natural biofuel, alongside a microwave-assisted variant (MA-SCS) of the same process. The crystalline structure of the as-prepared materials was examined by powder X-ray diffraction (PXRD), confirming formation of a single-phase monoclinic structure (JCPDS #24-423) with no detectable impurity phases in either sample. Average crystallite sizes, calculated using the Scherrer equation, were estimated at approximately 14 nm and 10 nm for the conventional and microwave-assisted samples, respectively, indicating that microwave irradiation promotes the formation of finer nanocrystallites. Photoluminescence (PL) spectroscopy under ultraviolet excitation ($\lambda ex = 358$ nm) revealed prominent Sm^{3+} emission bands at ~562 nm ($^4G_{5/2} \rightarrow {}^6H_{5/2}$), ~600 nm ($^4G_{5/2} \rightarrow {}^6H_{7/2}$), and ~645 nm ($^4G_{5/2} \rightarrow {}^6H_{9/2}$), producing characteristic orange-red emission. A significant enhancement in emission intensity was observed for the microwave-synthesised sample, attributable to improved crystallinity and reduced non-radiative defect density. These findings demonstrate that microwave-assisted green combustion synthesis constitutes a rapid, energy-efficient, and highly effective strategy for producing high-quality luminescent nanomaterials with superior optical performance.

Keywords: Gd$_2$MoO$_6$; Samarium doping; Green synthesis; aloe vera extract; Microwave combustion; Photoluminescence; Nanophosphors

INTRODUCTION

Luminescent materials activated by rare-earth (RE) ions have attracted extensive research interest owing to their widespread applications in solid-state lighting, photovoltaics, biomedical imaging, display technologies, and anti-counterfeiting systems [1,2]. The exceptional optical properties of RE-doped nanophosphors arise from well-shielded 4f-4f electronic transitions, which give rise to sharp, characteristic emission bands with high colour purity and long luminescence lifetimes.

Among the diverse host lattices explored for RE doping, molybdate-based compounds have garnered particular attention due to their chemical and thermal stability, wide optical band gap (~4 eV), and strong charge-transfer absorption in the near-ultraviolet (NUV) region arising from the highly polarisable [MoO$_4$]$^{2-}$ tetrahedra [3]. Gadolinium molybdate, Gd$_2$MoO$_6$, is a particularly promising host owing to its monoclinic crystal symmetry, efficient phonon-mediated energy transfer from the host to activator ions, and compatibility with a range of trivalent dopants. The Gd^{3+} sub-lattice, with its half-filled $^8S_{7/2}$ ground state, further facilitates efficient sensitisation of co-doped activator ions through resonant energy transfer mechanisms [4].

Samarium (Sm^{3+}) is a particularly attractive activator ion for warm-white and orange-red luminescent applications. Its characteristic emissions arise from electronic transitions from the $^4G_{5/2}$ excited multiplet to lower-lying $^6H_7$ levels, generating multiple bands in the 550–700 nm spectral window [5]. These properties make Sm^{3+}-doped molybdates candidates for applications in NUV-pumped LEDs, laser materials, and orange-emitting phosphors for display devices.

The physical and optical properties of nanophosphors are critically sensitive to the synthesis method employed. Conventional solution combustion synthesis (SCS) is a well-established, low-cost technique that exploits the exothermic redox reaction between metal nitrate oxidisers and an organic fuel to produce nanocrystalline powders in a single step [6]. However, the abrupt, uncontrolled heat release in conventional SCS often results in particle agglomeration, broad size distributions, and elevated defect concentrations. Microwave-assisted solution combustion synthesis (MA-SCS) offers a compelling alternative: volumetric and selective dielectric heating within the microwave cavity enables uniform temperature gradients, shorter ignition times, finer nanocrystallite formation, and improved phase purity [7].

In parallel, growing environmental awareness has motivated the replacement of conventional synthetic fuels (urea, citric acid, glycine) with plant-derived extracts. Aloe vera (Aloe barbadensis Miller) gel is particularly well-suited as a biofuel and capping agent due to its high content of polysaccharides (acemannan), reducing sugars, and polyhydric alcohols, which both sustain the combustion reaction and sterically passivate nanoparticle surfaces, limiting agglomeration [8].

Despite the substantial body of literature on RE-doped molybdates and on microwave-assisted synthesis separately, a systematic, side-by-side comparison of conventional and microwave-assisted green combustion using an identical aloe vera biofuel system for $Gd_2MoO_6:Sm^{3+}$ nanophosphors has not been reported. The present work addresses this gap by synthesising Gd_2MoO_6 and $Gd_2MoO_6:Sm^{3+}$ (0.5 mol%) via both routes under identical precursor and fuel conditions, and systematically comparing their structural and photoluminescent properties using PXRD and PL spectroscopy.

EXPERIMENTAL

Materials

Gadolinium(III) nitrate hexahydrate [$Gd(NO_3)_3\cdot 6H_2O$, 99.9%], ammonium molybdate tetrahydrate [$(NH_4)_6Mo_7O_{24}\cdot 4H_2O$, ≥99%], and samarium(III) nitrate hexahydrate [$Sm(NO_3)_3\cdot 6H_2O$, 99.9%] were used as received without further purification. All chemicals were of analytical reagent grade. Deionised water (resistivity ≥18 Ω·cm) was employed throughout.

Preparation of Aloe Vera Extract

Fresh aloe vera leaves were surface-cleaned with deionised water, and the inner gel (pulp) was carefully separated from the rind. Approximately 3 g of the gel was dispersed in 200 mL of deionised water and heated at 100 °C under continuous magnetic stirring for 2 h to extract the active organic constituents. The resultant pale-yellow solution was vacuum-filtered through Whatman No. 1 filter paper to remove particulate matter, yielding a clear, colloidal extract that was used immediately as the biofuel and capping agent.

Synthesis Procedure

The synthesis routes followed in this study are schematically depicted in Fig. 1. Two parallel methods were employed: conventional solution combustion (SCS) and microwave-assisted solution combustion (MA-SCS), both using the same precursor and biofuel system.

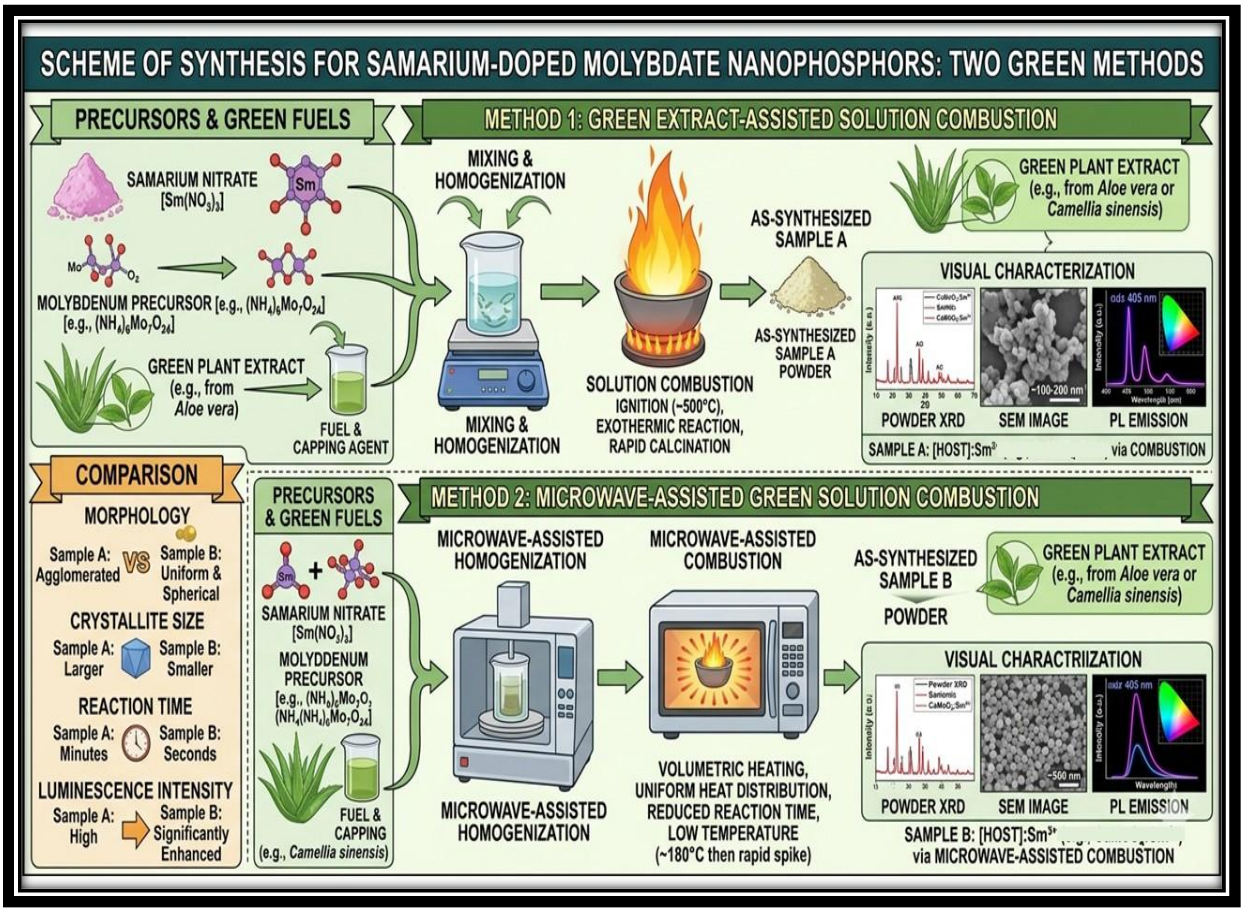

Fig. 1. Schematic representation of the synthesis routes for Sm^{3+}-doped Gd_2MoO_6 nanophosphors via (top) conventional green solution combustion and (bottom) microwave-assisted green solution combustion, with comparison of key structural and optical outcomes.

Conventional Solution Combustion (SCS)

Stoichiometric quantities of $Gd(NO_3)_3\cdot 6H_2O$ and $(NH_4)_6Mo_7O_{24}\cdot 4H_2O$, calculated according to the propellant chemistry formulation to achieve a fuel-to-oxidiser equivalence ratio (Φ) of unity, were dissolved in a minimum volume of deionised water. The aloe vera extract was incorporated as a natural fuel in a volume ratio optimised for complete combustion. For Sm^{3+}-doped samples, $Sm(NO_3)_3\cdot 6H_2O$ corresponding to 0.5 mol% relative to the Gd^{3+} site was added at this stage. The resulting homogeneous solution was placed in a pre-heated muffle furnace maintained at 600 °C. The solution underwent rapid dehydration followed by vigorous ignition, yielding a voluminous, porous powder within minutes.

Microwave-Assisted Combustion (MA-SCS)

An identical precursor and biofuel mixture was prepared as described above. The solution was transferred to a borosilicate glass vessel and subjected to microwave irradiation (domestic microwave oven, 2.45 GHz, 900 W) in 30-second intervals until ignition and complete combustion were achieved. The entire synthesis was completed within 3–5 minutes, after which the product was cooled to room temperature under ambient conditions. The microwave environment promotes dipolar and ionic polarisation of the solution, resulting in rapid, uniform volumetric heating that initiates combustion at significantly lower onset temperatures (~180 °C) compared to the conventional route.

CHARACTERISATION

The characterisation strategy employed in this study was designed to probe both the structural and photophysical properties of the synthesised nanophosphors, enabling a rigorous comparative evaluation of the two synthesis routes.

X-Ray Diffraction (XRD)

Phase identification and structural analysis were performed by powder X-ray diffraction (PXRD) using a PANalytical X'Pert Pro diffractometer equipped with Cu Kα radiation ($\lambda = 1.54056$ Å). Diffraction patterns were collected over a 2θ range of 10°–80° with a step size of 0.02° and a counting time of 2° min^{-1}. Phase identification was performed by matching experimental patterns against the JCPDS database.

Mean crystallite size (D) was estimated using the Scherrer equation:

$$D = K\lambda / (\beta \cos\theta)$$

where K is the Scherrer shape constant (0.9 for spherical crystallites), λ is the X-ray wavelength (1.5406 Å), β is the full width at half maximum (FWHM) of the most intense diffraction peak (corrected for instrumental broadening), and θ is the Bragg diffraction angle. Lattice parameters were refined by least-squares fitting using the monoclinic unit cell constraints appropriate to Gd_2MoO_6.

Photoluminescence Spectroscopy (PL)

Photoluminescence excitation (PLE) and emission (PL) spectra were acquired at room temperature using a Quanta Master 8450-22 Spectrofluorometer (Horiba Scientific) equipped with a 150 W Xe arc lamp source and photomultiplier tube (PMT) detector. PL emission spectra were collected under excitation at λ_{ex} = 358 nm, while PLE spectra were recorded monitoring the dominant emission peak at λ_{em} = 645 nm. Slit widths and integration times were maintained identical for both samples to enable direct intensity comparisons.

RESULTS AND DISCUSSION

Structural Analysis

The PXRD patterns recorded for both the SCS- and MA-SCS-synthesised $Gd_2MoO_6:Sm^{3+}$ (0.5 mol%) nanophosphors are shown in Fig. 2, along with the reference pattern from JCPDS card #24-423 for comparison.

All diffraction peaks in both samples can be unambiguously indexed to a monoclinic unit cell (space group $P2_1/a$), consistent with the standard Gd_2MoO_6 phase. No additional peaks attributable to impurity phases such as Gd_2O_3, MoO_3, or samarium oxide were detected, confirming the formation of phase-pure materials under both synthesis conditions and the successful lattice incorporation of Sm^{3+} ions at the Gd^{3+} crystallographic site. The absence of secondary phases is consistent with the similarity in ionic radii between Sm^{3+} (r = 0.958 Å, CN = 8) and Gd^{3+} (r = 1.053 Å, CN = 8), which favours isomorphous substitution without structural distortion.

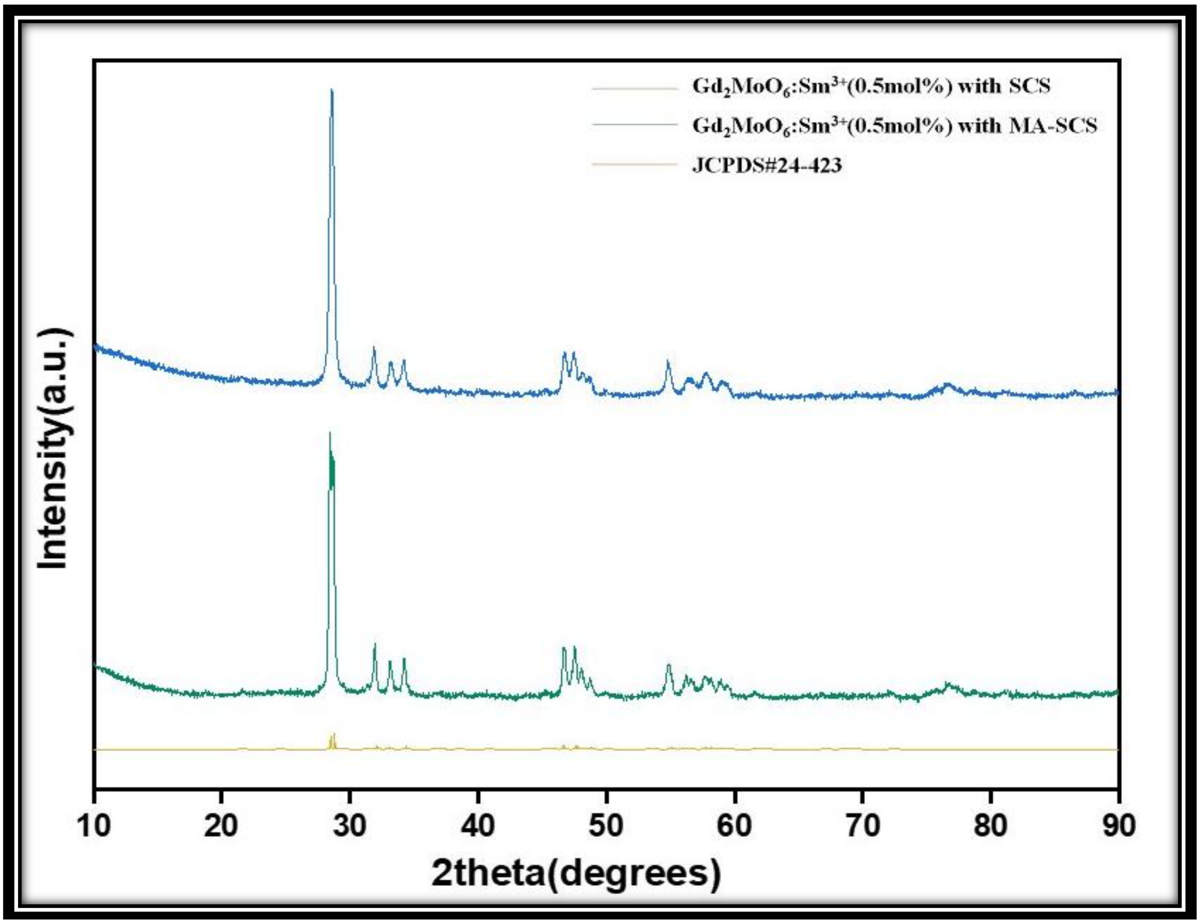

Fig. 2. Powder X-ray diffraction patterns of $Gd_2MoO_6:Sm^{3+}$ (0.5 mol%) synthesised by conventional SCS (green) and microwave-assisted MA-SCS (blue), with JCPDS #24-423 reference pattern shown in red. Broader peak profiles in the SCS sample indicate smaller coherent scattering domains.

A systematic broadening of diffraction peaks is clearly evident in the MA-SCS pattern compared to that of the SCS sample, indicative of reduced crystallite sizes in the microwave-processed material. Application of the Scherrer equation to the most intense peak at 2θ ≈ 28° yielded average crystallite sizes of approximately 14 nm (SCS) and 10 nm

(MA-SCS). The smaller crystallite size in the MA-SCS sample is attributed to the rapid, uniform heating characteristic of microwave processing, which promotes simultaneous nucleation of a large number of crystallisation centres, kinetically suppressing crystal growth. In contrast, conventional furnace heating in SCS involves a steep radial temperature gradient, favouring growth of a smaller number of larger crystallites.

The d-spacing values derived from peak positions showed excellent agreement with the reference card in both samples, confirming that Sm^{3+} incorporation does not significantly alter the lattice dimensions at the 0.5 mol% doping level. Minor peak shifts observed for MA-SCS relative to SCS may reflect subtle residual microstrain introduced during the rapid crystallisation process, which is consistent with the generally higher surface energy of smaller nanocrystallites.

Photoluminescence Properties

The PLE and PL emission spectra of $Gd_2MoO_6:Sm^{3+}$ (0.5 mol%) synthesised by both methods are presented in Figs. 3 and 4, respectively. Both figures reveal clearly resolved spectral features characteristic of Sm^{3+} ion transitions in a molybdate environment.

Photoluminescence Excitation Spectra

The PLE spectra recorded at λ_em = 645 nm (Fig. 3) exhibit a broad, intense absorption band centred around 350–380 nm, which is assigned to the charge-transfer (CT) transition from oxygen 2p orbitals to empty Mo 4d orbitals within the $[MoO_4]^{2-}$ tetrahedra of the host lattice. This broad CT band indicates efficient absorption of near-UV excitation energy by the molybdate host. Superimposed on the CT band, sharper features corresponding to direct 4f-4f absorption transitions of Sm^{3+} are also visible at longer wavelengths (~460–560 nm), confirming the incorporation of Sm^{3+} into the Gd_2MoO_6 host.

Critically, the MA-SCS sample (green curve) displays a markedly higher excitation intensity across the entire spectral range compared to the SCS sample (blue curve), with the most pronounced enhancement at the dominant CT band near 360 nm. This indicates that the microwave-processed sample possesses a higher density of structurally ordered $[MoO_4]^{2-}$ units capable of absorbing excitation photons, consistent with its superior crystallinity established from PXRD analysis.

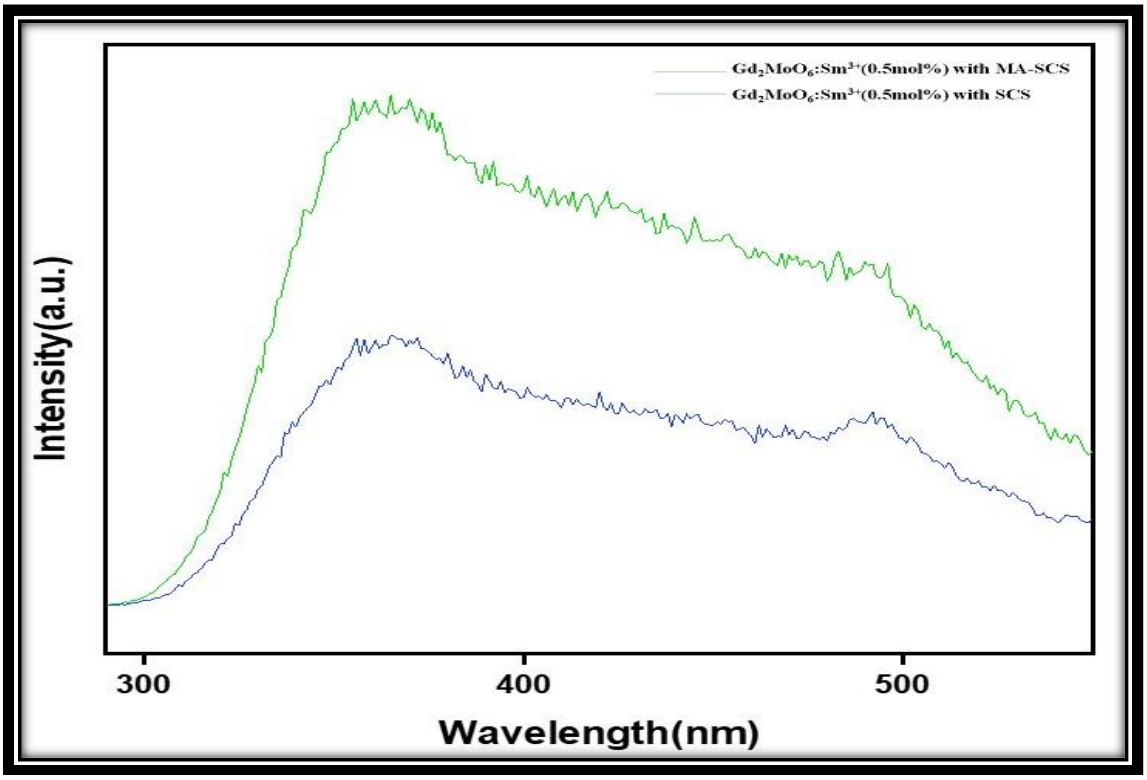

Fig. 3. Photoluminescence excitation (PLE) spectra of $Gd_2MoO_6:Sm^{3+}$ (0.5 mol%) monitored at λ_{em} = 645 nm for MA-SCS (green) and SCS (blue) samples. The broad charge-transfer band of the MoO_4^{2-} tetrahedra dominates the excitation profile, with Sm^{3+} 4f-level features visible at longer wavelengths.

Photoluminescence Emission Spectra

Upon excitation at 358 nm, both samples display a series of well-resolved emission peaks in the 550–700 nm region (Fig. 4), corresponding to the characteristic intraconfigurational ^{4}f-^{4}f transitions of Sm^{3+} from the thermally equilibrated $^4G_{5/2}$ excited state to lower $^6H_7$ multiplets:

- ~562 nm: $^4G_{5/2} \rightarrow {}^6H_{5/2}$ transition (green-yellow component)
- ~600 nm: $^4G_{5/2} \rightarrow {}^6H_{7/2}$ transition (dominant orange-red emission)
- ~645 nm: $^4G_{5/2} \rightarrow {}^6H_{9/2}$ transition (deep red component)

Additional weaker features near 710 nm ($^4G_{5/2} \rightarrow {}^6H_{11/2}$) are also discernible. The magnetic-dipole-allowed $^4G_{5/2} \rightarrow {}^6H_{5/2}$ transition is relatively insensitive to the crystal field environment, whereas the electric-dipole-allowed $^4G_{5/2} \rightarrow {}^6H_{7/2}$ transition is hypersensitive and follows the $\Delta J = \pm 2$ selection rule. The observed intensity ratio $I(^6H_{7/2}) / I(^6H_{5/2}) > 1$ indicates that Sm^{3+} occupies a non-centrosymmetric site in the Gd_2MoO_6 host, which enhances electric-dipole transition probabilities — a finding consistent with the monoclinic crystal symmetry ($P2_1/a$) of the host [9].

The MA-SCS sample exhibits a substantially higher overall PL emission intensity compared to the SCS sample across all Sm^{3+} emission peaks. This enhancement originates from several concurring factors: (i) the smaller crystallite size in MA-SCS provides a higher surface-area-to-volume ratio, increasing the density of Sm^{3+} luminescent centres accessible to excitation photons; (ii) the improved crystallinity reduces the concentration of structural defects (oxygen vacancies, lattice dislocations) that act as non-radiative recombination centres, thereby increasing the radiative quantum efficiency; (iii) the uniform heating in microwave combustion promotes more homogeneous distribution of Sm^{3+} dopant ions within the host lattice, reducing concentration quenching at local dopant-rich regions; and (iv) the more ordered $[MoO_4]^{2-}$ coordination environment in MA-SCS facilitates efficient host-to-activator energy transfer.

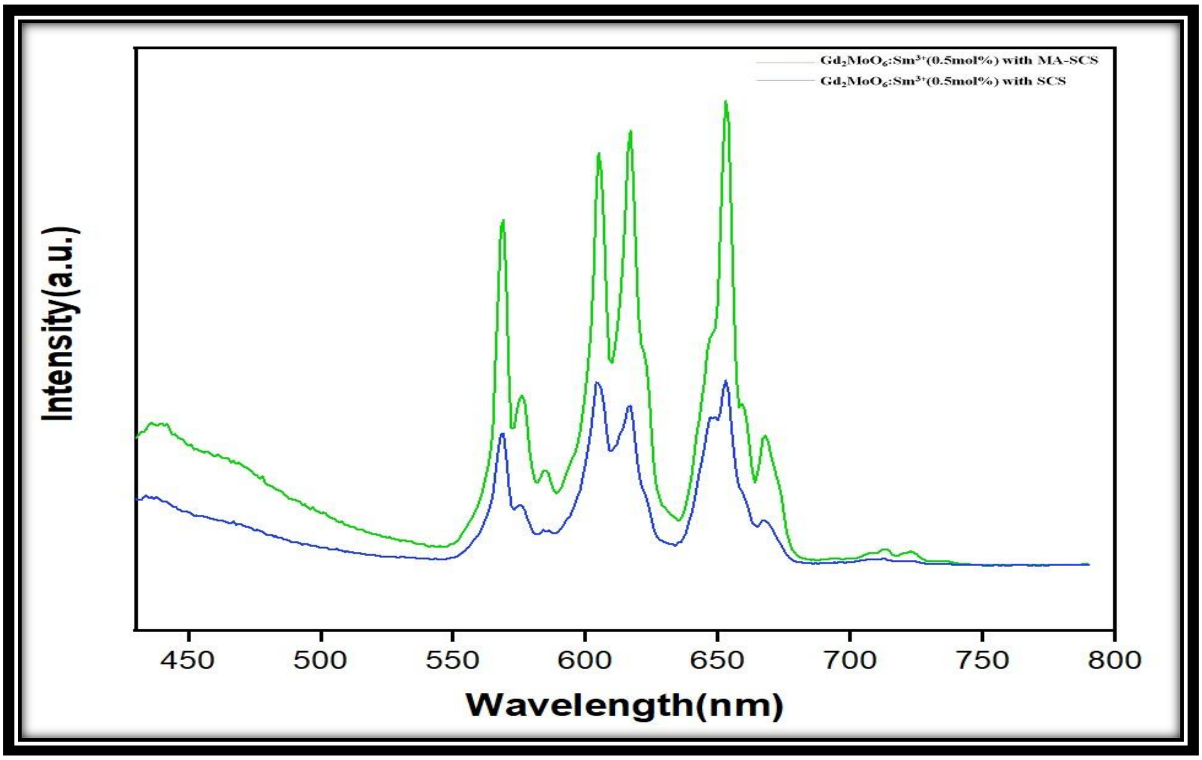

Fig. 4. Photoluminescence emission spectra (λ_{ex} = 358 nm) of $Gd_2MoO_6:Sm^{3+}$ (0.5 mol%) synthesised by MA-SCS (green) and SCS (blue). Emission peaks at ~562, ~600, and ~645 nm correspond to $^4G_{5/2} \rightarrow {}^6H_{5/2}$, $^4G_{5/2} \rightarrow {}^6H_{7/2}$, and $^4G_{5/2} \rightarrow {}^6H_{9/2}$ transitions of Sm^{3+}, respectively.

Decay Lifetime

The decay behavior of the phosphor was studied by measuring the luminescence decay profile at the characteristic emission wavelength under suitable excitation. A triple-exponential function (ExpDec3) best described the experimental decay curve, indicating that there are several relaxation pathways involved in the emission process. The decay profile can be expressed by,

$$I(t) = A_1 e^{-t/\tau_1} + A_2 e^{-t/\tau_2} + A_3 e^{-t/\tau_3}$$

where $I(t)$ is the luminescence intensity at time t, A_1, A_2, and A_3 are pre-exponential constants, while τ_1, τ_2, τ_3 signify the decay time constants associated with different decay channels. The average lifetime was calculated using the weighted average lifetime relation:

$$\tau_{avg} = \frac{A_1 {\tau_1}^2 + A_2 {\tau_2}^2 + A_3 {\tau_3}^2}{A_1 \tau_1 + A_2 \tau_2 + A_3 \tau_3}$$

The estimated average decay lifetime is 3.16 µs, which reveals efficient radiative emission and a relaxation process on the order of microsecond as shown in fig.5.

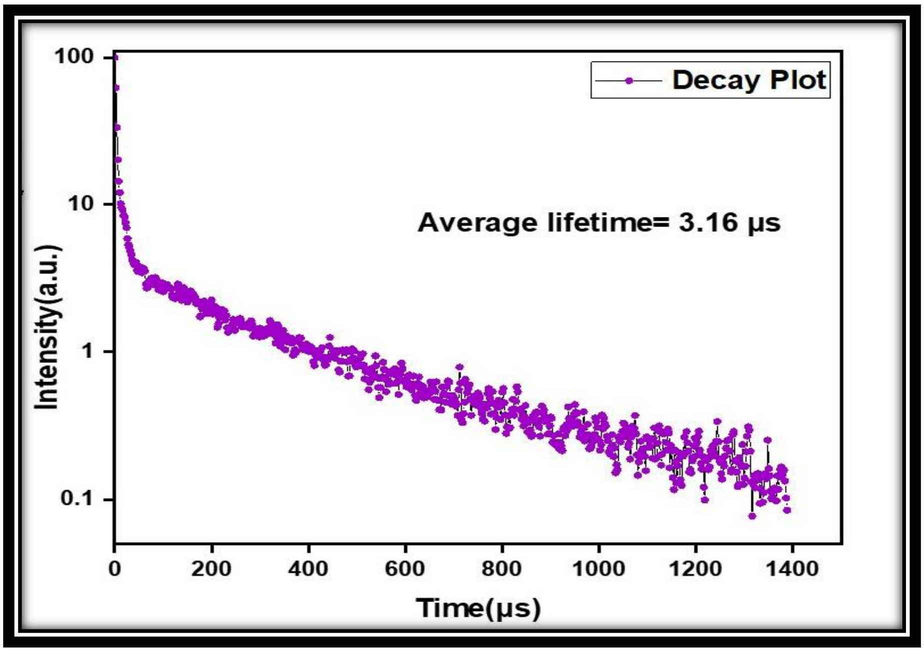

Fig. 5. Decay curve of Gd_2MoO_6:Sm^{3+} (0.5 mol%) nanophosphor.

CIE coordinates and CCT

The chromaticity properties of the synthesized phosphors were analyzed by CIE 1931 chromaticity diagram and the corresponding correlated color temperature (CCT) values were calculated from the emission spectra . The CIE chromaticity coordinates of the phosphor obtained by solution combustion synthesis (SCS) method were found to be (0.416, 0.286) with the calculated CCT value of 2034 K as depicted in fig. 6. Similarly, the CIE coordinate of the phosphor prepared by microwave-assisted solution combustion synthesis (MASCS) route was found to be (0.423, 0.278) with a CCT value of 1834 K as represented in fig. 7. The obtained chromaticity coordinates for both the samples are located in the warm color region. The comparatively lower CCT value of the sample obtained from MASCS indicates a relatively warmer emission behavior. The slight variation in the chromaticity coordinates between the two synthesis pathways suggests that the preparation method affects the emission properties and color output of the phosphor material.

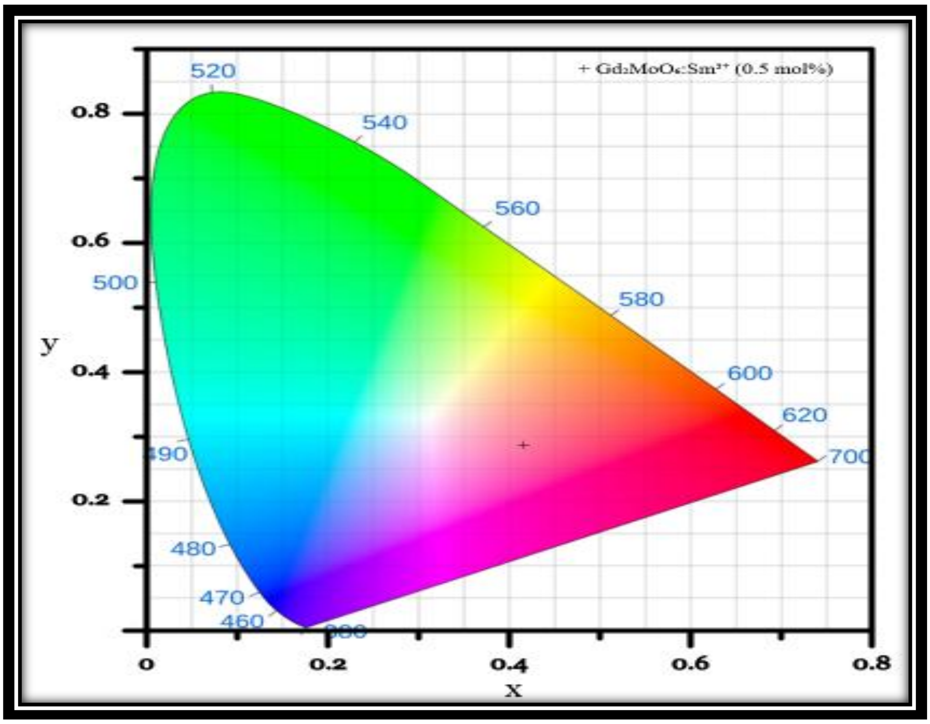

Fig. 6. CIE coordinates of Gd_2MoO_6:Sm^{3+} (0.5 mol%) nanophosphor synthesized by SCS

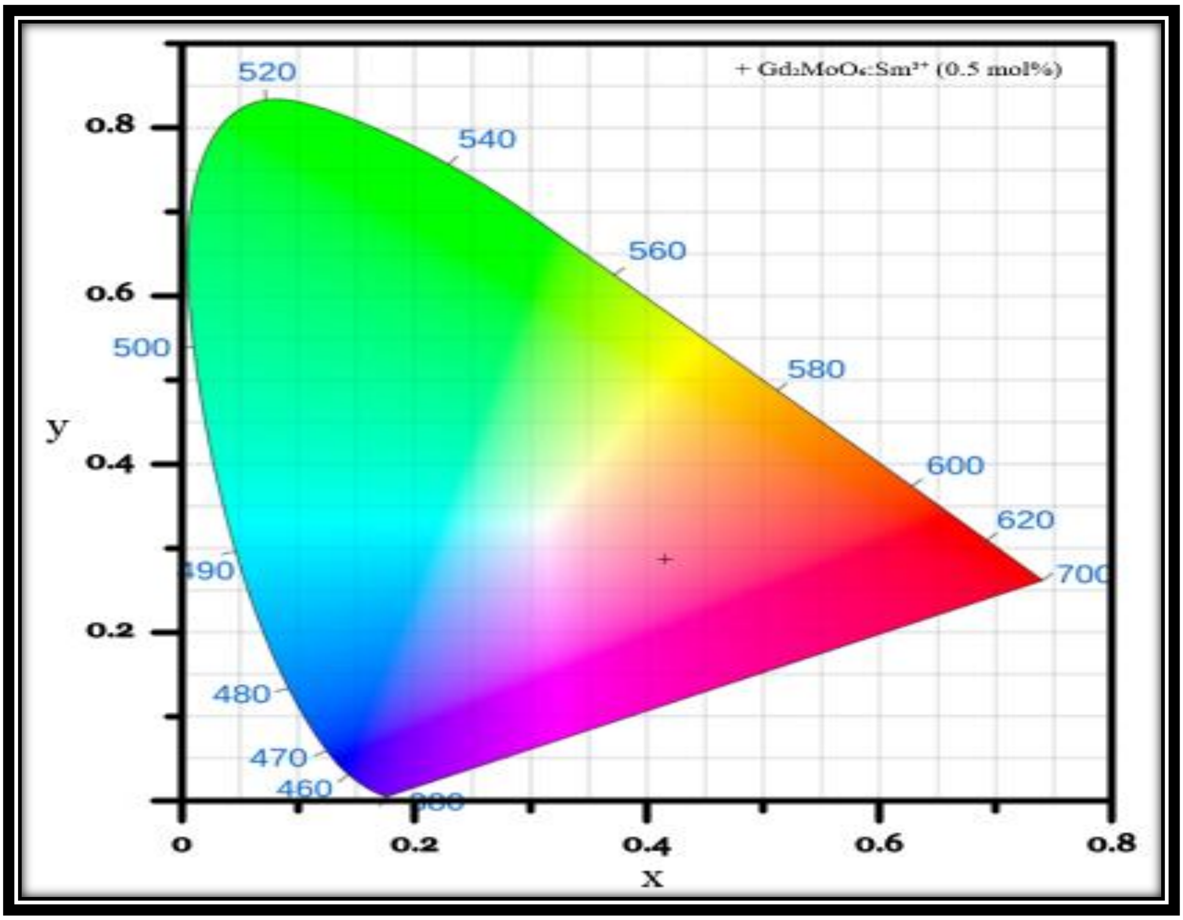

Fig. 7. CIE coordinates of $Gd_2MoO_6{:}Sm^{3+}$ (0.5 mol%) nanophosphor synthesized by MA-SCS

Role of Aloe Vera Biofuel

The choice of aloe vera extract as a natural biofuel has a multifaceted influence on the synthesis outcome. The polysaccharide-rich composition of aloe vera gel provides both combustible organic matter (fuel function) and a colloidal stabilising medium (capping agent function). The polyhydric alcohols and reducing sugars present in the extract generate sufficient exothermic energy to sustain the oxidative combustion of metal nitrate precursors, while simultaneously coordinating to nascent nanoparticle surfaces through oxygen-donor functional groups, retarding excessive particle growth and agglomeration. The relatively mild, diffuse character of biofuel-driven combustion — compared to concentrated inorganic fuels — produces a more gradual heat release profile that may further contribute to nanocrystal homogeneity. Optimisation of aloe vera concentration is essential to avoid incomplete combustion (yielding carbonaceous residues) or over-fuelling (resulting in excessively exothermic, uncontrolled reactions), both of which can degrade luminescence performance.

Comparative Evaluation

Table 1 summarises the key structural and photophysical parameters for both synthesis routes.

Table 1. Comparative structural and luminescent parameters of $Gd_2MoO_6{:}Sm^{3+}$ nanophosphors synthesised by conventional (SCS) and microwave-assisted (MA-SCS) green combustion.

Parameter	Conventional SCS	Microwave-Assisted (MA-SCS)
Reaction duration	20–30 min	3–5 min
Phase purity	Single phase (JCPDS #24-423)	Single phase (JCPDS #24-423)
Crystallite size (Scherrer)	~14 nm	~10 nm
Crystallinity	Moderate	Superior
Particle morphology	Agglomerated	Finer, more uniform
PL emission intensity	Lower	Significantly higher

Dominant emission (λmax)	~645 nm (orange-red)	~645 nm (orange-red)
Energy efficiency	Moderate (furnace heating)	High (microwave dielectric)

CONCLUSION

This study has demonstrated the successful synthesis of phase-pure Gd_2MoO_6 and $Gd_2MoO_6:Sm^{3+}$ (0.5 mol%) nanophosphors by two parallel green combustion strategies — conventional solution combustion (SCS) and microwave-assisted solution combustion (MA-SCS) — both employing aloe vera extract as an environmentally benign biofuel. The key conclusions drawn from this comparative investigation are as follows:

1. Phase-pure monoclinic Gd_2MoO_6 (JCPDS #24-423) was obtained under both synthesis conditions, confirming that aloe vera-mediated green combustion — whether conventional or microwave-assisted — is an effective route to single-phase molybdate nanophosphors.
2. Microwave-assisted synthesis yielded significantly finer nanocrystallites (~10 nm) compared to conventional combustion (~14 nm), attributable to the rapid, homogeneous volumetric heating unique to microwave irradiation, which favours simultaneous nucleation over sequential crystal growth.
3. The MA-SCS samples exhibited substantially enhanced photoluminescence emission across all Sm^{3+} transitions ($^4G_{5/2} \rightarrow {}^6H_{5/2}$ at ~562 nm, $^4G_{5/2} \rightarrow {}^6H_{7/2}$ at ~600 nm, and $^4G_{5/2} \rightarrow {}^6H_{9/2}$ at ~645 nm). This enhancement is attributed to the combined effects of improved crystallinity, reduced non-radiative defect density, more uniform dopant distribution, and enhanced host-to-activator energy transfer efficiency.
4. The aloe vera biofuel acts dually as a combustion fuel and a nanoparticle surface-capping agent, contributing to phase purity, reduced agglomeration, and morphological uniformity. Its renewable, non-toxic nature aligns with principles of sustainable synthesis.
5. The microwave-assisted green combustion approach reduces total synthesis time to under 5 minutes and avoids high-temperature furnace infrastructure, offering a practical, scalable, and energy-efficient pathway for the production of high-quality rare-earth luminescent nanomaterials.

Collectively, these results establish $Gd_2MoO_6:Sm^{3+}$ nanophosphors prepared via MA-SCS as promising candidates for NUV-pumped warm-white or orange-red LED phosphors, and validate microwave-assisted biofuel combustion as a broadly applicable platform for the green fabrication of high-performance functional nanomaterials. Future investigations may profitably explore the concentration dependence of Sm^{3+} luminescence, the influence of biofuel-to-oxidiser ratio on particle morphology, and the potential for co-doping with sensitiser ions (e.g., Eu^{3+}, Tb^{3+}) to further augment emission efficiency.

ACKNOWLEDGMENT

Ms Diksha gratefully acknowledges the Council of Scientific and Industrial Research (CSIR), New Delhi, India, for financial support in the form of a Junior Research Fellowship (JRF, Award No: 09/1279(19751)/2024-EMR-I).

AI-Assistant Statement

The authors used Artificial Intelligence tools for grammar improvement and preparation of the scheme image. No AI tool was used for scientific analysis, interpretation of results, or conclusions. All content was reviewed and approved by the authors in accordance with the Journal's policy and publishing ethics guidelines.

REFERENCES

1. Sun, Y., Feng, W., Yang, P., Huang, C., & Li, F. (2015). The biosafety of lanthanide upconversion nanomaterials. Chemical Society Reviews, 44(6), 1509–1525.
2. Rodrigues, J. (2023). Luminescent materials: synthesis, characterization and applications. Applied Sciences, 13(15), 8705.
3. Mondal, M., et al. (2016). Enhanced frequency upconversion in $Ho^{3+}/Yb^{3+}/Li^{+}$: $YMoO_4$ nanophosphors for photonic and security ink applications. Journal of Applied Physics, 120(23).
4. Yengkhom, D. D., et al. (2025). Ce^{3+}-sensitized $SrF_2:Tb^{3+}$ nanophosphors for anticounterfeiting and fingerprint detection. Sensors & Diagnostics, 4, 63–74.
5. Al-Jawad, S. M., & Ismail, M. M. (2017). Characterization of Mn, Cu, and (Mn, Cu) co-doped ZnS nanoparticles. Journal of Optical Technology, 84(7), 495–499.
6. Navami, D., et al. (2021). Green emitting $CaZrO_3:Tb^{3+}$ nanophosphor for fingerprint detection. Optical Materials, 122, 111474.
7. Lian, J., et al. (2024). $InGaZnO_4:Eu^{3+}$ phosphor for fingerprint and security ink applications. Solid State Sciences, 157, 107702.

8. Chaithra, C. K., et al. (2025). Carbon dots on $CaAl_2O_4$ phosphor for anti-counterfeiting and sensing. Journal of Luminescence, 280, 121111.
9. Navya, N., et al. (2024). Carbon dots embedded perovskite phosphor for thermometry and data protection. Materials Today Sustainability, 27, 100840.
10. Lavanya, D. R., et al. (2022). $La_2Zr_2O_7:Eu^{3+}$ nanophosphors for fingerprint visualization. Surfaces and Interfaces, 29, 101803.
11. Swathi, B. N., et al. (2023). $Sr_9Al_6O_{18}:Pr^{3+}$ nanophosphors for fingerprint detection. ACS Applied Nano Materials, 6, 21322–21339.
12. Fischer, S., et al. (2015). Upconverting core-shell nanocrystals with high quantum yield under low irradiance: On the role of isotropic and thick shells. Journal of Applied Physics, 118(19).
13. Lin, P., et al. (2023). Dual-emissive phosphors for anti-counterfeiting. Inorganic Chemistry Frontiers, 10, 5178–5185.
14. Sivasankarapillai, V. S., et al. (2020). Recent advancements in the applications of carbon nanodots. Nanoscale Advances, 2(5), 1760–1773.
15. Purushothaman, B., & Song, J. M. (2021). Ag_2S quantum dot theragnostics. Biomaterials Science, 9, 51–69.